Imperfections of the Thermohaline Circulation: Latitudinal Asymmetry and Preferred Northern Sinking*

HENK A. DIJKSTRA

Institute for Marine and Atmospheric Research Utrecht, Utrecht University, Utrecht, Netherlands

J. DAVID NEELIN

Department of Atmospheric Sciences and Institute of Geophysics and Planetary Physics, University of California, Los Angeles, Los Angeles, California

(Manuscript received 2 March 1998, in final form 31 March 1999)

ABSTRACT

The present Atlantic thermohaline circulation is dominated by deep water formation in the north despite the fact that surface buoyancy forcing has relatively modest latitudinal asymmetry. Many studies have shown that even with buoyancy forcing that is symmetric about the equator, spontaneous symmetry breaking can produce a single overturning cell with intense sinking in the north. This occurs by salt advection at sufficiently large freshwater forcing. In this symmetry-breaking case, a southern-sinking solution and a symmetric solution are also possible. A simple coupled ocean–atmosphere model of the zonally averaged thermohaline circulation is used to examine the effect of latitudinal asymmetries in the boundary conditions. The greater continental area in the Northern Hemisphere, combined with the slight asymmetry in the observed freshwater flux, induce a strong preference for the northern-sinking solution. Examining the relation to the solution under symmetric conditions, the salt-advection mechanism still acts to enhance the overturning circulation of the northern-sinking branch, but multiple equilibria are much less likely to occur within the realistic parameter range. The most plausible shift between equilibria for paleoclimate applications would be between a strong northern-sinking branch and a weak northern-sinking branch that is an asymmetric version of the thermally driven solution. However, this is possible only in a very limited range of parameters. There is a substantial parameter range where the northern-sinking branch is unique. The role of the fractional region of air–sea interaction at each latitude is substantial in producing north–south asymmetry.

1. Introduction

One of the issues of great importance to climate research is why the oceanic thermohaline circulation has the pole to pole configuration, sinking in the northern Atlantic, which is presently observed, and whether it can be perturbed into other stable equilibrium states as an explanation for paleoclimate variability (e.g., Stommel 1961; Broecker et al. 1985; Marotzke and Willebrand 1991; Stocker and Wright 1991a,b; Stocker et al. 1992a,b; Broecker 1993; Weaver et al. 1991, 1993; Weaver and Hughes 1994; Winton 1997 and references therein). The possibility that such transitions might occur in association with anthropogenic climate change (Manabe and Stouffer 1993, 1995; Stocker and Schmittner 1997) adds concern to this question.

The zonally averaged oceanic overturning circulation is mainly forced at the ocean–atmosphere interface by heat and freshwater fluxes. In considering a coupled ocean–atmosphere system, the fundamental forcing is the incoming solar radiation, while the other components of the surface heat budget, as well as the net freshwater flux, are negotiated between ocean and atmosphere. The latitudinal dependence of the zonally averaged forcing in the observed climate is relatively symmetric about the equator, compared to the strong latitudinal asymmetry of the observed circulation. One may ask how a nearly symmetric buoyancy flux gives rise to a circulation pattern with such strong asymmetry as observed. A number of studies have considered a possible answer to this question: asymmetric circulation patterns can originate from spontaneous symmetry breaking of a symmetric flow driven by perfectly latitudinally symmetric buoyancy flux about the equator.

* Institute of Geophysics and Planetary Physics Contribution Number 4892.

Corresponding author address: Henk A. Dijkstra, Institute for Marine and Atmospheric Research Utrecht, Department of Physics and Astronomy, Utrecht University, Princetonplein 5, 3584 CC Utrecht, Netherlands.
E-mail: dijkstra@phys.uu.nl

This leads to multiple equilibria, with asymmetric solutions coexisting with symmetric solutions.

The existence of multiple equilibria in thermohaline-driven flows has been demonstrated in a hierarchy of models ranging from box models (Stommel 1961; Welander 1986; Huang et al. 1992; Nakamura et al. 1994), to zonally averaged, two-dimensional models (e.g., Marotzke et al. 1988; Quon and Ghil 1992; Stocker and Wright 1991a,b; Stocker et al. 1992a,b; Thual and McWilliams 1992), to ocean general circulation models (GCMs) with specified atmospheric boundary conditions and simplified atmospheric feedbacks (Bryan 1986; Weaver and Sarachik 1991; Marotzke and Willebrand 1991; Weaver et al. 1993; Power and Kleeman 1993; Zhang et al. 1993; Hughes and Weaver 1994; Rahmstorf 1994, 1995) and coupled ocean–atmosphere GCMs (Manabe and Stouffer 1988). Reviews are given in Weaver and Hughes (1992) and Rahmstorf et al. (1995). Mixed boundary conditions—in which sea surface temperature (SST) is restored toward or prescribed to an equilibrium value, while surface freshwater flux is independent of salinity—are central to the primary physical mechanism producing multiple equilibria. Under these boundary conditions, a salinity perturbation at the surface is advected with the flow, whereas SST perturbations are kept relatively small. The mechanism is most clearly seen in the case of latitudinally symmetric boundary conditions (Marotzke et al. 1988; Quon and Ghil 1992, 1995; Thual and McWilliams 1992; Vellinga 1996; Dijkstra and Molemaker 1997). The mechanism of symmetry breaking originates from an advective feedback that enables an antisymmetric density perturbation to destabilize the symmetric thermally driven flow. The surface flow of the associated pole to pole circulation perturbation advects saline water toward one pole, increasing the density there, and reinforcing the antisymmetric density perturbation.

Bifurcation diagrams showing the solutions as a function of key control parameters have been constructed in box models and two-dimensional models. Such diagrams are useful in understanding the relationships among regimes where multiple equilibria or unique equilibrium states occur. Bifurcation diagrams have so far been computed for symmetric boundary conditions (Quon and Ghil 1992; Thual and McWilliams 1992; Dijkstra and Molemaker 1997). Under small symmetric freshwater flux forcing (with net evaporation at the equator and net precipitation near the poles), the circulation is thermally dominated and because of the equator to pole negative temperature gradient, a symmetric two-cell circulation results. When the freshwater flux is increased, this symmetric solution undergoes a pitchfork bifurcation and asymmetric pole to pole solutions come into existence.

Although the studies above identify the physics of the multiple equilibria in these idealized models, a natural next step is to consider what happens when the constraints of symmetry are replaced by more realistic boundary conditions. Any asymmetric effect will cause the pitchfork bifurcations responsible for symmetry breaking to disappear. Hence, the branches of both pole to pole solutions will disconnect in phase space and the new domain of existence of each solution depends on the strength of particular asymmetry. The study of such a break up of a symmetric bifurcation diagram by introduction of asymmetries in the system is often termed ''imperfection theory.'' Recently (Dijkstra and Neelin 1999), we have considered the impact on the solution structure of the ''flux-correction'' procedures that are often used in models in an attempt to produce a realistic climatology in imperfect models. It was noted that slight asymmetries, in that case introduced by the flux-correction procedure, could give a substantial change in the regimes of multiple equilibria.

A number of studies in two- and three-dimensional models have found multiple stable equilibria existing at a given set of parameter values for boundary conditions with asymmetry about the equator (e.g., Stocker et al. 1992a; Marotzke and Willebrand, 1991; Hughes and Weaver 1994; Rahmstorf 1995, 1996). Because these models are solved by time integration, it has been difficult to place the multiple equilibria in the larger context of a bifurcation diagram, although a nice example of inferring a partial bifurcation diagram from hysteresis effects in an ocean GCM is provided by Rahmstorf (1995). In the present paper, we address systematically how the thermohaline circulation (THC) bifurcation diagram is distorted from the latitudinally symmetric case to a case with more realistic boundary conditions. This can assist in the theoretical interpretation of the branches encountered in other models, and in assessing the factors affecting robustness of multiple equilibria. It contributes also to answering the question of why the present thermohaline circulation is so strongly asymmetric, showing how latitudinal asymmetries contribute to a preference for the northern sinking branch.

A zonally averaged ocean model coupled to an energy balance atmosphere model is solved with the branch-following techniques of Dijkstra and Molemaker (1997). The energy-balance atmosphere alleviates the problem of overly strong constraint on large-scale SST fields encountered when Newtonian cooling boundary conditions are used in ocean models (Tziperman et al. 1994; Rahmstorf and Willebrand 1995; Marotzke and Pierce 1997). It also permits us to relate the latitudinal asymmetry affecting heat fluxes directly to latitudinal asymmetry in the configuration of the continents, specifically through the fraction of ocean at a given latitude circle. This fraction affects the heat flux boundary condition on the ocean as follows. When the ocean is a small fraction of the latitude circle, warming of SST by poleward ocean heat transport has a relatively small effect on the atmospheric temperature. Thus the high-latitude ocean tends to be more strongly cooled when the ocean fraction is small (in presence of a poleward heat trans-

port, if there is no ocean transport, SST is exactly the same as the land temperature). The second source of asymmetry considered here is in the freshwater flux. In the real climate system, this arises from the asymmetry in continental configuration affecting atmospheric water vapor transports. Simple parameterizations of this flux have been considered, for example, by Stocker et al. (1992a), Fanning and Weaver (1996), and Nakamura et al. (1994). The dependence of precipitation is difficult to capture with confidence, and Hughes and Weaver (1996) have shown that the temperature dependence of evaporation has only a modest effect. Here we simply use estimates of the observed freshwater flux and examine the impact of latitudinally asymmetric versions versus a symmetrized version.

For simplicity, we work in the context of a single, Atlantic-like basin. We thus omit asymmetric effects that arise due to connection of the Southern Ocean to the Pacific and Indian basins. Stocker et al. (1992a), who first developed a zonally averaged ocean coupled to an energy-balance atmosphere, consider the connection to these other basins, as do Marotzke and Willebrand (1991) and Hughes and Weaver (1994) in ocean GCMs. All assume that each basin is of constant longitudinal width, so our source of asymmetry is complementary. By our configuration, solutions with sinking in the northern Pacific or both northern basins are obviously excluded. However, we can examine effects on the northern-sinking versus southern-sinking pole to pole branches, termed ''conveyor belt'' and southern-sinking solutions by Marotzke and Willebrand. We can also offer a possible perspective on the large differences between the multiple equilibria encountered in these studies and some of those found by Rahmstorf (1994, 1995, 1996), in terms of the bifurcation diagram for the asymmetric case.

2. Formulation of the coupled ocean–atmosphere model

We consider a zonally averaged Boussinesq ocean model of the Atlantic basin of meridional scale L and constant depth H coupled to a one-dimensional energy balance atmosphere model. Formulations of both models are well known and the uncoupled versions have been shown capable of capturing the most important features of the thermohaline circulation and zonally averaged atmospheric heat budget. Previous studies that use coupling to an energy balance atmosphere include Stocker et al. (1992a), Chen and Ghil (1996), and Winton (1997).

The energy balance model (North et al. 1981) is used to model the surface temperature ϑ of the atmosphere. Its governing equation is

$$C_a \frac{\partial \vartheta}{\partial t} = Q_s - (A + B\vartheta) + \frac{\partial}{\partial y}\left(D_a \frac{\partial \vartheta}{\partial y}\right) - \gamma Q_{oa}, \quad (1a)$$

with meridional coordinate y. The boundary conditions are

$$y = 0, L: \quad \frac{\partial \vartheta}{\partial y} = 0. \quad (1b)$$

In the equation above, C_a is the (very small) thermal inertia of the atmosphere, A and B are two constants parameterizing the effect of longwave radiative cooling, D_a parameterizes the effect of baroclinic eddies on the meridional heat transport, γ is the fraction of the earth covered by the ocean basin, and Q_{oa} is the (downward) ocean–atmosphere heat flux. The latter is positive when heat is transferred from the atmosphere to the ocean. The shortwave radiation at the top of the atmosphere is prescribed as

$$Q_s(y) = Q_a^* S_a(y/L), \quad (2)$$

with $Q_a^* = \frac{1}{4}\Sigma_0(1 - \alpha)$, where Σ_0 is the solar constant, and α the planetary albedo. The function $S_a(y) = 1 - 0.239[3(2y - 1)^2 - 1]$ represents the latitudinal dependence of the shortwave radiation (North et al. 1981).

A 2D Boussinesq model is used to model the zonally averaged ocean circulation within the basin (Quon and Ghil 1992; Cessi and Young 1992; Dijkstra and Molemaker 1997). The equations for the meridional velocity v, vertical velocity w, pressure p, density ρ, temperature T, and salinity S are given by

$$\rho_0 \frac{Dv}{dt} = -\frac{\partial p}{\partial y} + a_H \frac{\partial^2 v}{\partial y^2} + a_V \frac{\partial^2 v}{\partial z^2}, \quad (3a)$$

$$\rho_0 \frac{Dw}{dt} = -\frac{\partial p}{\partial z} + a_H \frac{\partial^2 w}{\partial y^2} + a_V \frac{\partial^2 w}{\partial z^2} - \rho g, \quad (3b)$$

$$\frac{\partial v}{\partial y} + \frac{\partial w}{\partial z} = 0, \quad (3c)$$

$$\frac{DT}{dt} = \kappa_H \frac{\partial^2 T}{\partial y^2} + \kappa_V \frac{\partial^2 T}{\partial z^2}, \quad \text{and} \quad (3d)$$

$$\frac{DS}{dt} = \kappa_H \frac{\partial^2 S}{\partial y^2} + \kappa_V \frac{\partial^2 S}{\partial z^2}. \quad (3e)$$

In the equations above, D/dt is the material derivative, ρ_0 indicates a reference density, and a linear equation of state $\rho = \rho_0[1 - \alpha_T(T - T_0) + \alpha_S(S - S_0)]$ is assumed. Moreover, the quantities $A = a/\rho_0$ and κ are (eddy) diffusivities of momentum and heat/salt. The subscripts V and H denote vertical and horizontal properties, respectively. In this model setup, no convective adjustment is applied, since it is known that the overall solution structure is the same (Vellinga 1996) as the model used here, but artificial equilibria may be introduced by the adjustment procedure (Vellinga 1998).

The boundary conditions for temperature and salinity at the ocean surface ($z = H$) become

$$\rho_0 C_p \kappa_V \frac{\partial T}{\partial z} = Q_{oa} \tag{4a}$$

$$\kappa_V \frac{\partial S}{\partial z} = F_0 F_S(y). \tag{4b}$$

In the latter boundary condition, the conversion between the freshwater flux and a (virtual) salt flux has been made, with F_0 indicating its amplitude and $F_S(y)$ its spatial structure. Salinity and heat fluxes are supposed to be zero at the bottom and lateral boundaries and slip conditions are also applied at these boundaries. In this way, the boundary conditions become

$$\begin{aligned} &y = 0, L: \quad \frac{\partial T}{\partial y} = \frac{\partial S}{\partial y} = 0, \qquad v = 0, \qquad \frac{\partial w}{\partial y} = 0; \\ &z = 0: \quad \frac{\partial T}{\partial z} = \frac{\partial S}{\partial z} = 0, \qquad w = 0, \qquad \frac{\partial v}{\partial z} = 0; \quad \text{and} \\ &z = H: \quad w = 0, \qquad \frac{\partial v}{\partial z} = 0. \end{aligned} \tag{5}$$

The formulation of the downward heat flux Q_{oa} requires some care in interpretation since ϑ is the atmospheric surface temperature. As considered by Haney (1971), the net downward heat flux into the ocean Q_{oa} can be approximated by

$$Q_{oa} = Q_1 + Q_2(\vartheta - T) \tag{6a}$$

if it is assumed that the air–sea temperature difference is small. The quantity Q_1 models the net downward heat flux of solar radiation across the ocean surface, minus the upward flux of longwave radiation and latent heat from an ocean surface at a temperature ϑ. The term Q_2 represents the net upward flux of longwave radiation and sensible and latent heat per degree excess of ocean surface temperature T over the atmospheric surface temperature ϑ. The downward heat flux Q_{oa} into the ocean obtained from the surface heat parameterization, as in Haney (1971), leads to

$$Q_{oa} = Q_o^* S_o(y) + \mu_{oa}(\vartheta - T), \tag{6b}$$

where $S_o(y)$ is a shape function strongly related to $S_a(y)$. We note some important physical and quantitative differences between this formulation of the air–sea exchange used here and some implementations of coupled energy balance models. For (6b) the heat flux reaching the ocean surface has a large solar component, with the remainder related to air–sea interaction. If φ is interpreted as surface air temperature, then this solar contribution to the heat flux has to be taken into account. This is consistent with Stocker et al. (1992a) but contrasts with Chen and Ghil (1996) and their Eq. (2), which effectively assumes that the solar heat flux is absorbed in the atmosphere.

We nondimensionalize the equations by using scales H and L for the horizontal and vertical length, $U = \kappa_H/L$ for horizontal velocity, HU/L for vertical velocity, ΔT and $\Delta S/\lambda$ for temperature (ocean and atmosphere) and salinity (where $\lambda = \alpha_S \Delta S/\alpha_T \Delta T$ is the buoyancy ratio), and L^2/κ_H for time. Furthermore, the pressure is eliminated in the equations (3), and a streamfunction ψ and a vorticity ζ are introduced. This leads to the following equations governing the coupled system:

$$\eta_a \frac{\partial \vartheta}{\partial t} = S_a(y) - (\alpha_a + \beta_a \vartheta) + \zeta_a \frac{\partial^2 \vartheta}{\partial y^2} - \gamma(y)[q_f S_o(y) + \mu(\vartheta - T)], \tag{7a}$$

$$\mathrm{Pr}^{-1} \frac{D\zeta}{dt} = \frac{\partial^2 \zeta}{\partial z^2} + \frac{A_H}{A_V} \delta^2 \frac{\partial^2 \zeta}{\partial y^2} + \mathrm{Ra}\left(\frac{\partial T}{\partial y} - \frac{\partial S}{\partial y}\right), \tag{7b}$$

$$\zeta = -\left[\frac{\partial^2 \psi}{\partial z^2} + \delta^2 \frac{\partial^2 \psi}{\partial y^2}\right], \tag{7c}$$

$$\frac{DT}{dt} = \frac{\partial^2 T}{\partial z^2} + \frac{\kappa_H}{\kappa_V} \delta^2 \frac{\partial^2 T}{\partial y^2}, \quad \text{and} \tag{7d}$$

$$\frac{DS}{dt} = \frac{\partial^2 S}{\partial z^2} + \frac{\kappa_H}{\kappa_V} \delta^2 \frac{\partial^2 S}{\partial y^2}. \tag{7e}$$

The boundary conditions (5) remain unchanged, and the boundary conditions at the ocean–atmosphere boundary become

$$\begin{aligned} &z = 1: \quad w = 0; \qquad \frac{\partial v}{\partial z} = 0; \\ &\frac{\partial T}{\partial z} = \eta_f[q_f S_o(y) + \mu(\vartheta - T)]; \qquad \frac{\partial S}{\partial z} = \sigma F_S(y). \end{aligned} \tag{8}$$

The function F_S in (8) is the salt flux latitudinal distribution, and the parameter σ monitoring its strength will be used as a control parameter. The dimensionless parameters in the equations are given by

$$\begin{aligned} &\eta_a = \frac{C_a \Delta T \kappa_H}{L^2 Q_a^*}, \qquad \alpha_a = \frac{A}{Q_a^*}, \qquad \beta_a = \frac{B\Delta T}{Q_a^*}, \\ &\xi_a = \frac{D_a \Delta T}{Q_a^* L^2}, \qquad \eta_f = \frac{HQ_a^*}{\rho_o C_p \kappa_V \Delta T}, \qquad q_f = \frac{Q_o^*}{Q_a^*}, \\ &\mu = \frac{\mu_{oa} \Delta T}{Q_a^*}, \qquad \delta = \frac{H}{L}, \qquad \mathrm{Ra} = \frac{HL^2 g \alpha_T \Delta T}{A_H \kappa_H}, \\ &\lambda = \frac{\alpha_S \Delta S}{\alpha_T \Delta T}, \qquad \mathrm{Pr} = \frac{A_H}{\kappa_H}, \quad \text{and} \quad \sigma = \frac{F_0 H \lambda}{\kappa_V \Delta S}. \end{aligned} \tag{9}$$

The values of the dimensional quantities together with the standard values of the dimensionless parameters are given in Table 1. It appears that the value of Ra is too large to perform calculations on a manageable resolution. It is also known that the bifurcation behavior is not very sensitive to Ra, once its value is large enough (Dijkstra and Molemaker 1997). Therefore, a standard value of $\mathrm{Ra} = 10^4$ was taken in the equations below, and the values of the parameters of the atmosphere mod-

TABLE 1. Standard values of dimensional and dimensionless parameters.

Parameter	Value
Dimensional parameter	
L	1.5×10^7 m
H	4.0×10^3 m
C_a	10^7 W m^{-2} K^{-1} s
D_a	10^{13} W K^{-1}
Q_a^*	240 W m^{-2}
κ_V	7.3×10^{-5} m^2 s^{-1}
g	9.8 m s^{-2}
ΔT	1.0 K
Q_o^*	180 W m^{-2}
$\rho_0 C_p$	4.2×10^6 J K^{-1} m^{-3}
α_T	1.6×10^{-4} K^{-1}
α_S	7.6×10^{-4}
A	216 W m^{-2}
B	1.5 W m^{-2}
κ_H	10^3 m^2 s^{-1}
A_H	2.5×10^5 m^2 s^{-1}
A_V	1.8×10^{-2} m^2 s^{-1}
ΔS	1.0
μ_{oa}	10 W m^{-2}
F_0	1.0×10^{-6} m s^{-1}
Dimensionless parameters	
η_a	1.85×10^{-7}
q_f	0.75
η_f	3.1×10^3
Ra	1.0×10^4
Pr	250
β_a	6.25×10^{-3}
α_a	0.9
μ	0.042
ξ_a	1.85×10^{-4}
δ	2.67×10^{-4}
σ	250
λ	4.75

el were slightly adjusted (to values in Table 1) to get the temperatures in the realistic range.

The steady equations (7)–(8) are discretized on a nonequidistant grid using a finite volume method, and solutions to the resulting nonlinear algebraic system of equations are found following Dijkstra and Molemaker (1997). The same nonequidistant 60×30 grid is used, which was confirmed to give sufficiently accurate results.

3. Results

a. The ''perfect'' bifurcation diagram

For the standard values of the parameters as in Table 1 and constant $\gamma = \gamma_0 = 0.125$ for all latitudes, the bifurcation diagram is shown in Fig. 1 for an idealized freshwater flux shape

$$F_S = \cos\left[2\pi\left(y - \frac{1}{2}\right)\right], \tag{10}$$

as used in earlier studies (Quon and Ghil 1992; Dijkstra and Molemaker 1997). The streamfunction value in the center point (ψ) of the domain is used as an index of the flow. If the solution is symmetric, the value of $\psi = 0$ and hence the symmetric solutions all collapse onto the zero line in Fig. 1. This value is plotted against $\sigma_r = \sigma/\sigma_B$, where $\sigma_B = 80.0$ is the value of σ at the pitchfork bifurcation, and hence this bifurcation is located at exactly $\sigma_r = 1$.

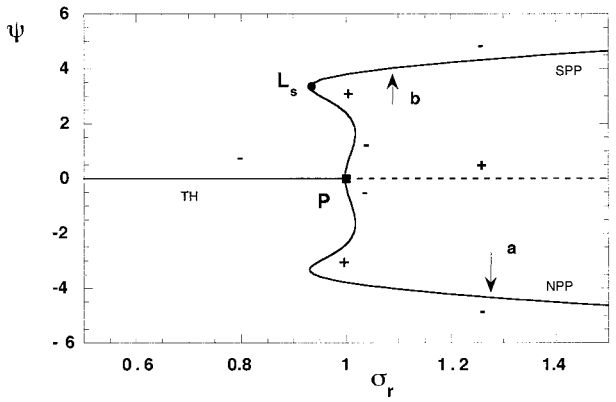

FIG. 1. Bifurcation diagram as a function of the parameter controlling the strength of freshwater flux σ_r, for standard values of the parameters given in Table 1, for the case of latitudinally symmetric boundary conditions. On the vertical axis, the streamfunction value ψ at the center of the grid ($x = 0.5$, $y = 0.5$) is shown. Points P and L denote pitchfork bifurcation and limit point. NPP and SPP denote northern and southern pole to pole circulation branches, and TH the thermally driven branch. Points marked *a* and *b* correspond to Fig. 2 and $-$ (+) signs indicate stable (unstable) branches.

The linear stability of the solutions has not been analyzed explicitly for two reasons. Apart from the occurrence of Hopf bifurations, the stability properties can be derived from generic behavior of the system, combined with previous knowledge of the bifurcation diagrams (Dijkstra and Molemaker 1997). Although any oscillatory instability would be of interest, the unstable steady states are still important to the statistically steady states. Stability along the branches to stationary perturbations is indicated by markers along the branches, $-$ (+) indicating an stable (unstable) branch of solutions.

The thermally dominated solution, labeled the TH-branch, loses stability at the pitchfork bifurcation $P(\sigma_r = 1.0)$. Two mirror-image solution branches appear that have asymmetric circulation patterns, labeled NPP and SPP, in notation similar to that used by Thual and McWilliams (1992). They are associated over much of the parameter range with pole to pole circulations, with sinking at northern and southern boundaries, respectively. Fully developed pole to pole solutions are present when σ_r has passed the limit point L_s (at $\sigma_r = 0.93$). At marked points along these branches (Fig. 1), patterns of the streamfunction, the sea surface temperature, and atmospheric surface temperature are plotted in Fig. 2. These show the familiar pole to pole solutions giving an asymmetry of approximately 4°C in the temperature difference between the North and South Poles. Over the

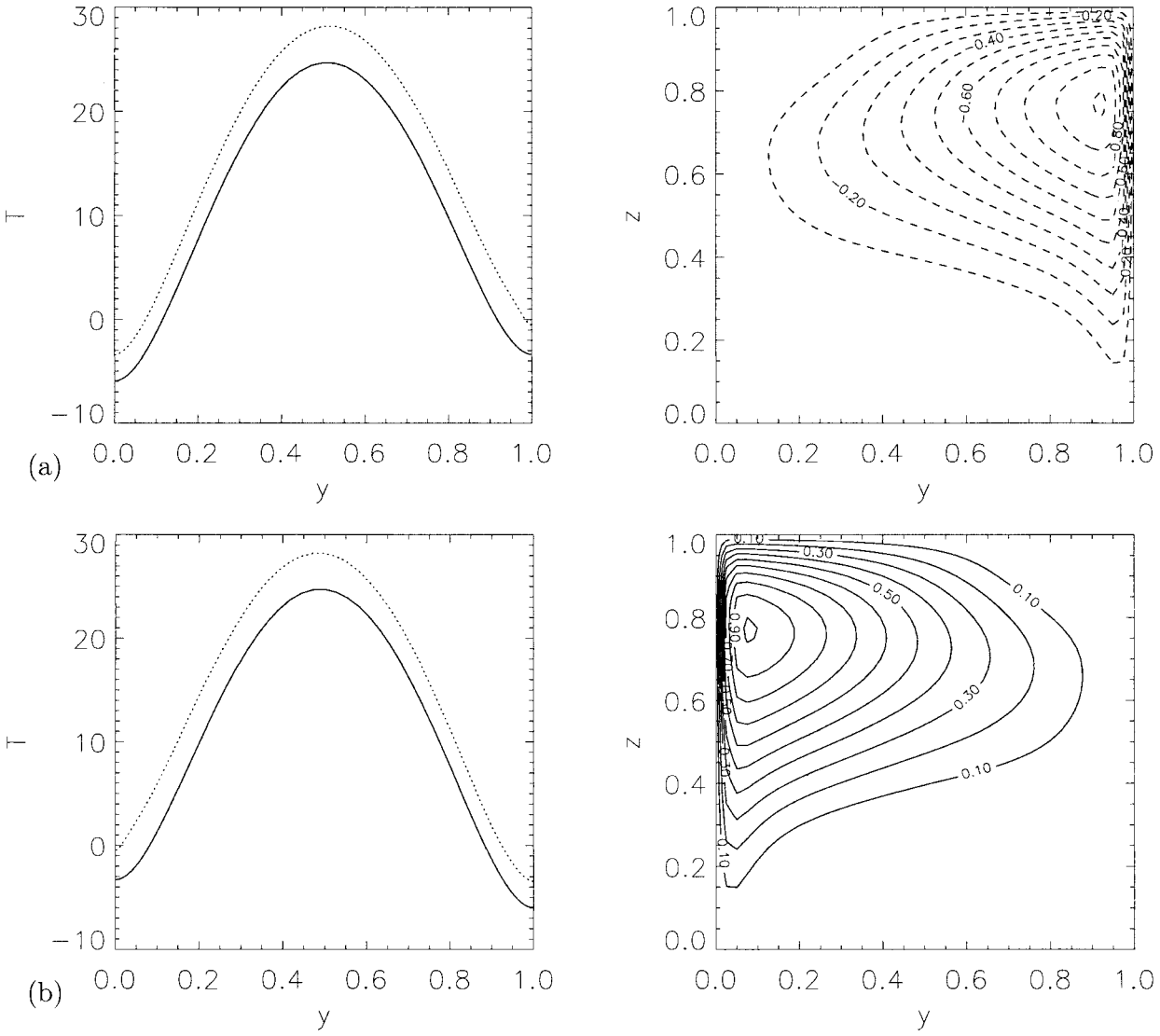

FIG. 2. In the left panels, the SST (dotted curve) and atmospheric surface temperature (solid curve) at marked points in Fig. 1 are plotted. In the right panels, contour plots of the streamfunction are shown, scaled by its absolute maximum; contour levels are with respect to this maximum. The coordinate y is a dimensionless coordinate that is related to the dimensional coordinate $y^* = Ly$, where L is the meridional extent of the domain. Hence, if the domain on the sphere is from $[-\theta_0, \theta_0]$, then $L = 2\theta_0 r_0$, where r_0 is the radius of the earth. (a) NPP branch, $\sigma_r = 1.27$. (b) SPP branch, $\sigma_r = 1.09$.

whole domain, the ocean is a few degrees warmer than the atmosphere, in agreement with observations (e.g., Peixoto and Oort 1992).

b. Effects of continental asymmetry on air–sea interaction

The most fundamental latitudinal asymmetry about the equator is the distribution of continents. Here we idealize this to a latitudinally asymmetric meridional distribution of the relative area of ocean and land at each latitude. The relative area γ of the Atlantic Ocean with respect to the total area in a sector of 5° latitude, computed from areas on a map, is shown in Fig. 3a. The value at 60°N is about 0.13, while at 40°S, between South America and a point just south of the Southern tip of Africa, it is about 0.24. In Fig. 3a, the value of 0.25 is simply continued southward. However, the expanse of the Indian Ocean could equally be included, and in the Antarctic Circumpolar Ocean, the observed value of γ is 1.0. While it is clear that the latitudinal asymmetry in γ in Fig. 3a is quite conservative, it becomes a modeler's decision how much of the Southern Ocean fraction to attribute to the Atlantic overturning circulation in an Atlantic-only configuration as used here. Likewise in the northern regions, the areas where air–sea interaction is important—that is, the regions of active deep convection—are much smaller than the total

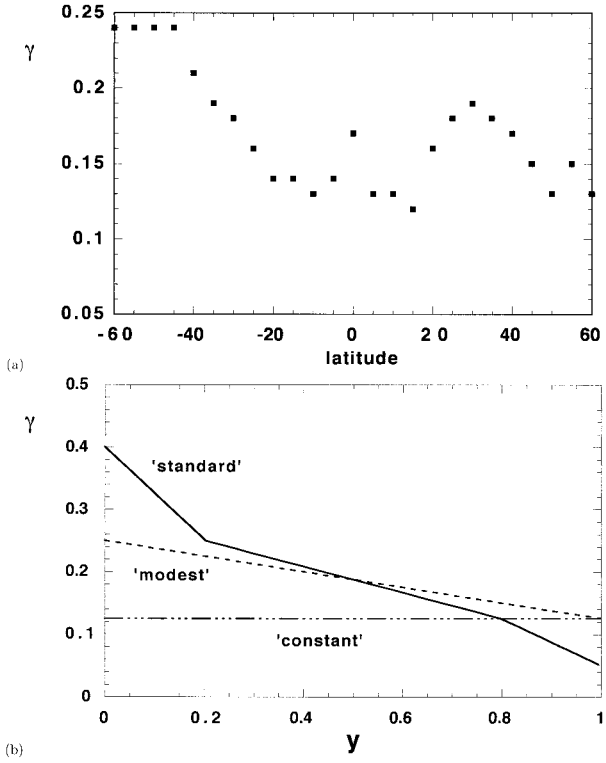

FIG. 3. (a) The ratio γ of the area of the Atlantic Ocean to total area within sectors of 5° latitude as determined from simple area calculations. (b) Shape of γ used in the standard case and ''modest'' asymmetry case, the former including an increase in the area of air–sea interaction due to the presence of the Southern Ocean. For completeness, the value of γ_0 used in the symmetric case is also plotted. The coordinate y is a dimensionless coordinate that is related to the dimensional coordinate $y^* = Ly$, where L is the meridional extent of the domain. Hence, if the domain on the sphere is from $[-\theta_0, \theta_0]$, then $L = 2\theta_0 r_0$, where r_0 is the radius of the earth.

ocean fraction of 0.125, so we consider a case in which γ is further reduced near the northern boundary.

To give a feeling for the impact of the choices of continental asymmetry in a roughly realistic but simplified context, we show results from two asymmetric continental configurations. We first use a ''modest asymmetry'' configuration, given by the simple approximation

$$\gamma(y) = 0.25 - 0.125y, \tag{11}$$

where y is in the range [0, 1] over the basin. This case has smaller than observed asymmetry about the equator. A more realistic (although still simplified) asymmetry is given by our ''standard case'' continental configuration, shown in Fig. 3b. The larger region of air–sea interaction in the Southern Ocean and the reduced area in the Northern Ocean are taken into account by a piecewise linear shape of γ. At the southern boundary the value of γ is taken as 0.4, which effectively assumes that heat transports in the Atlantic overturning circulation influence the atmosphere over 40% of the latitude circle, while the rest of the latitude circle is passive and

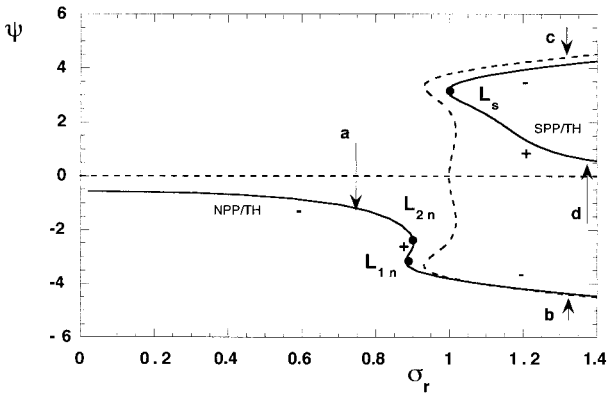

FIG. 4. Bifurcation diagram (solid curves) for the case of modest asymmetry in the continental configuration [γ given by the linear function (11)]. The symmetric continental configuration case of Fig. 1 is given for comparison (dashed curves). Freshwater flux is symmetric with idealized latitudinal dependence, as in (10).

behaves like a land surface. Asymmetry due to the Southern Ocean is likely underestimated by this, but the effects prove already substantial. From this value, γ decreases to 0.25 at $y = 0.2$, followed by a further linear decrease to 0.125 at $y = 0.8$. In the northern segment, γ decreases to 0.05 at the northern boundary, equivalent to about 20° of longitude.

To determine the impact on the structure of the solutions in Fig. 1, we recomputed the branches of the bifurcation diagram using the asymmetric continental configurations. Figure 4 shows the case with modest continental asymmetry given by (11). As soon as $\gamma(y)$ becomes asymmetric with respect to the equator, the pitchfork bifurcation connecting the symmetric and asymmetric branches breaks up. The stable symmetric TH solution connects to the NPP solution and this branch is therefore labeled NPP/TH. Similarly, the unstable TH solution connects to the SPP branch and the resulting branch is labeled SPP/TH. For clarity, the symmetric bifurcation diagram (dashed curves) is also plotted in Fig. 4. At large σ_r, the asymmetric case branches approach those of the symmetric case, but at more realistic values of σ_r, close to the original pitchfork bifurcation, the branches have moved rapidly away from the pitchfork as asymmetry is introduced.

The solutions at the NPP/TH branch (plotted in Fig. 5 at the labeled points in Fig. 4) have hardly changed for large σ_r (compare Figs. 2a and 5b). When σ_r is decreased, a small interval of σ_r remains where there exist multiple asymmetric equilibria caused by the two limit points L_{1n} and L_{2n} (Fig. 4). At smaller σ_r, on the NPP/TH branch (Fig. 5a), there is substantial asymmetry with the northern overturning cell being both more intense and extending over a larger region. However, there is still a two-cell structure, which is a signature of the symmetric TH solution. Similar signatures can be seen in the solution plotted in Fig. 5d, which shows the connection between the unstable part of the

TH branch and the SPP branch due to the imposed asymmetry. Of interest is the shift in the limit point L_s in Fig. 4 that is now located near $\sigma_r = 1$. The solution change (compare Figs. 5c and 2b) shows that a larger area of air–sea interaction in the south has increased both the temperature of the ocean and atmosphere in the southern part of the basin, increasing the buoyancy in the upper part of the ocean. Hence, a larger value of σ is necessary to maintain the southern-sinking solution.

Based on the previous result, the shift in the limit points L_s is expected to become even stronger when the value of γ increases in the south or further decreases in the north. For the standard case continental configuration (Fig. 3b), the bifurcation diagram in Fig. 6 shows that indeed L_s occurs at even larger σ ($\sigma_r = 1.07$) than that in Fig. 4. The flow patterns along the branches show similar features to those in Fig. 5 and are not shown. However, both limit points on the NPP/TH branch have disappeared, implying that there are no multiple equilibria below $\sigma_r = 1.07$. A consequence of this is that there is a substantial parameter range where the northern-sinking branch is strong, and is similar to the NPP branch in the symmetric case, but where there is no steady state corresponding to the SPP branch. In physical terms, the salt advection mechanism, which produces multiple equilibria in the symmetric case, is acting to enhance the overturning in the NPP/TH branch but is not strong enough to produce a southern-sinking branch. The NPP/TH branch in this range (about $\sigma_r = 0.7$ to L_s in Fig. 6) appears similar to cases in the range above L_s, but the global behavior of the system is qualitatively different in the two ranges, since one range has a unique equilibrium and the other has two equilibria.

4. Asymmetric air–sea interaction and freshwater flux

In the previous results, the zonally averaged freshwater flux over the Atlantic basin has been idealized as a cosine profile. A better estimate of this flux is obtained by using data from Baumgartner and Reichel (1975), Zaucker et al. (1994), and from the Oort (1983) climatology. The average of the results obtained from these three datasets gives the dash-dotted curve in Fig. 7a. Its symmetric component is shown as the solid curve, and the dashed curve is the difference between the two. The latter curve suggests that asymmetry is introduced mainly in the Tropics and subtropics.

When one adds an offset to the symmetric curve such that its integral over the basin is zero, the resulting profile is well fitted by

$$F_S^s(y) = -\cos[2\pi(y - 1/2)] + 2.4e^{-([10(y-1/2)]/\pi)^2} - 0.24\pi^{1/2}\mathrm{Erf}(5). \quad (12a)$$

(Weijer et al. 1999). In the following results, the starting point is the symmetric F_S shape (12a) as drawn in Fig. 7b as the solid curve. To obtain asymmetric freshwater fluxes, an idealized approximation to the asymmetric component of the freshwater flux is introduced (still requiring its integral over the basin to be zero). The particular shape used is

$$F_S(y) = F_S^s(y) - pe^{-20(y-1/2)^2}[\sin(4\pi y) + 1.2\sin(2\pi y)], \quad (12b)$$

where a homotopy parameter p is used to control the strength of the asymmetric component. Profiles of the freshwater flux shape are shown for a different p in Fig. 7b. Inspecting the estimated flux in Fig. 7a and the different profiles in Fig. 7b, a value of p between 0.25 and 0.75 corresponds to a reasonable asymmetry of the freshwater flux.

For the shape of F_S as in (12b) with $p = 0$—that is, symmetric freshwater flux—the bifurcation structures are shown in Fig. 8 both for the symmetric case $\gamma = 0.125$ (dashed curves) as well as for the standard continental configuration (γ as in Fig. 3b). The value of $\sigma_B = 461.35$ at the pitchfork bifurcation in the symmetric case. This value is larger than the estimated ''realistic'' value (Table 1) of about 250 which is derived from the amplitude of the fresh-water flux in Fig. 7a. In the bifurcation diagrams below, again $\sigma_r = \sigma/\sigma_B$ and hence, for the symmetric forcing, the pitchfork bifurcation is located again at $\sigma_r = 1.0$. The most realistic regime is thus roughly in the vicinity of $\sigma_r = 0.5$ or 0.6. The relative distance between this pitchfork and the limit point L_s (at $\sigma_r = 0.55$) is significantly increased compared to that in Fig. 1.

Information on the solutions is provided in Fig. 9 for several marked points along the branches. The northern-sinking solution under symmetric forcing (Fig. 9a) shows a much more intense flow at greater depth, which is absent in the patterns shown earlier. This indicates a more bulk-driven flow; that is, the buoyancy production is divided more homogeneously over the flow region. Similar comments apply to the southern-sinking solution (Fig. 9b). Both solutions exhibit a ''dip'' in the streamlines just south (Fig. 9a) or just north (Fig. 9b) of the equator, which is related to the local precipitation maximum near the equator (Fig. 7a).

In the bifurcation diagram for the continental configuration of the standard case (γ as in Fig. 3b), the NPP/TH branch at large σ_r is not strongly modified (Fig. 8). For example, the solution in Fig. 9c is, although at smaller σ_r, nearly the same as in Fig. 9a. The limit points L_{1n} and L_{2n} continue to exist and consequently, a region of multiple equilibria persists with simultaneous stable patterns shown in Figs. 9c,d. For the southern-sinking branch, the qualitative result is again that the limit point L_s moves to larger $\sigma_r = 0.68$ caused by the same effect as discussed above: the rise in temperature (compare Figs. 9b and 9e) in the southern part of the basin requires stronger salt forcing to maintain the branch. Although this shift in limit point is fairly large, there does not appear to be strong preference for the NPP/TH branch yet, and multiple equilibria of both northern and south-

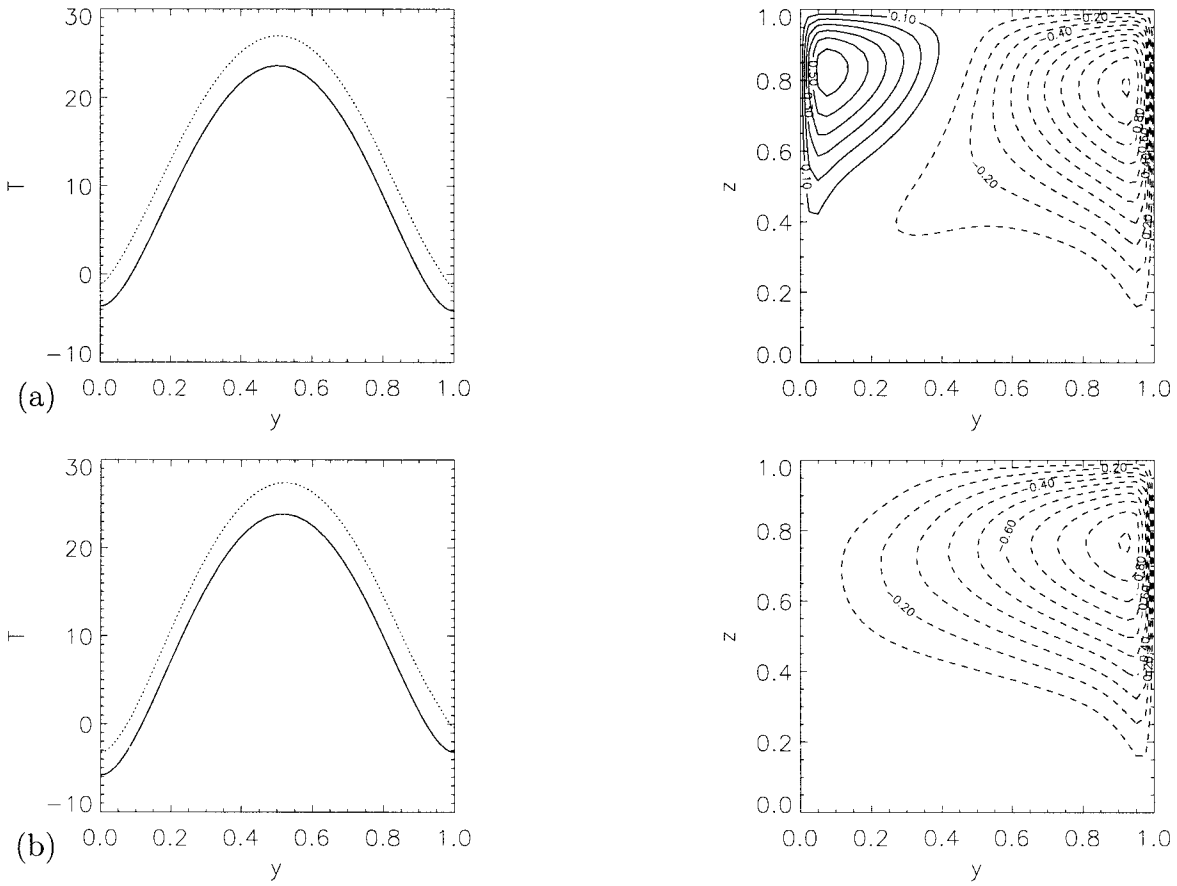

FIG. 5. Solutions at marked points in Fig. 4. Left panels show SST (dotted curve) and atmospheric surface temperature (solid curve). Right panels shows latitude–depth plots of the streamfunction, scaled by its absolute maximum; contour levels are with respect to this maximum. (a) NPP/TH branch, $\sigma = 0.71$. (b) NPP/TH branch, $\sigma = 1.34$. (c) SPP/TH branch, $\sigma = 1.34$. (d) SPP/TH branch, $\sigma = 1.38$.

ern polar sinking are still possible for σ_r larger than 0.68. There exists a small regime (between $\sigma_r = 0.68$ and 0.73) where three stable equilibria are possible, as in the symmetric case, but where the central, TH-like, solution is asymmetric, with a stronger northern cell.

Figure 10 shows the corresponding bifurcation diagram for $p = 0.4$, that is, a reasonable asymmetry in the fresh water flux (Fig. 7b). The diagram for $p = 0$ is plotted again for reference. With asymmetric freshwater flux, the southern part of the basin is freshened with respect to the northern part, which tends to favor northern sinking. The limit point L_s of the southern-sinking branch thus moves even farther to the right. For $p = 0.2$, the dot marks the position of this limit point; and for $p = 0.4$, the limit point is located $\sigma_r = 0.87$. Hence, both asymmetries cooperate in limiting the interval of σ_r for which the southern-sinking branch exists. For larger p eventually the southern-sinking branch moves quite far from the region of ''realistic'' σ_r values, which is around $\sigma_r \approx 0.6$. In Fig. 10, for $p = 1.0$ this branch lies outside the plotted region.

At the same time, and because of the salinification of the northern part of the basin, the limit points in the northern-sinking branch move to smaller values of σ_r. This opens a window in σ_r where a unique northern-sinking branch appears. Hence, both asymmetric air–sea interaction and asymmetric freshwater flux induce a preference for the northern-sinking branch. However, for $p = 0.4$ and in the range of realistic σ_r, multiple equilibria still occur due to the limit points L_{1n} and L_{2n}. This structure with a pair of saddle-node bifurcations is similar to the structure inferred by Rahmsdorf (1995) in an ocean GCM coupled to a simplified energy-balance atmosphere model. It echoes the structure that occurs in the original Stommel (1961) two-box model (which had only one hemisphere). The patterns of the two stable equilibria are shown in Figs. 11a and 11b. Transitions between these states due to finite amplitude perturbations are possible in this regime. It is significant that the asymmetric TH branch (Fig. 11b) has almost a pole to pole domain, but with weaker overturning circulation than the NPP solution. These transitions would thus be between states that both have northern sinking but sim-

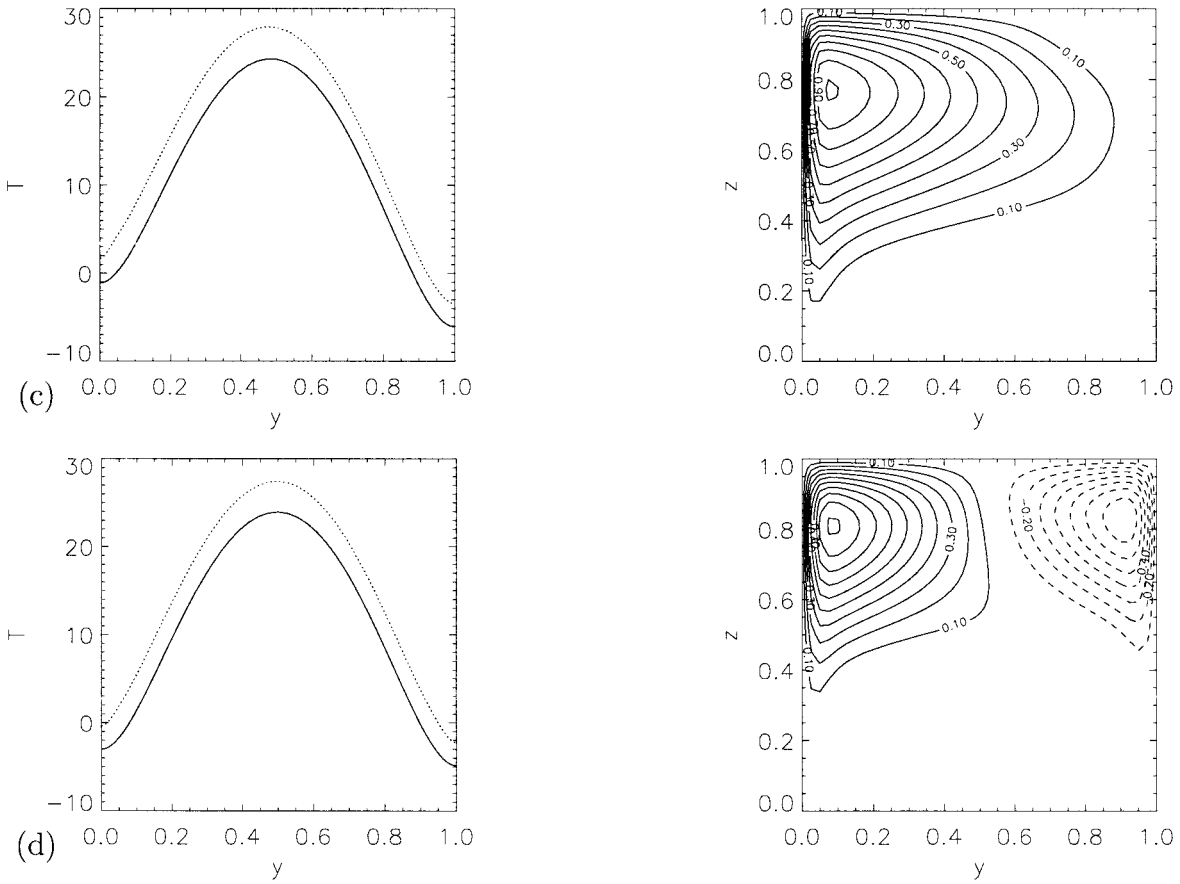

FIG. 5. (*Continued*)

ply weaker and stronger values. The zonally averaged SST differs by less than 1 K between the two solutions.

When $p = 1$—that is, strong asymmetry in the freshwater flux—both limit points have shifted to small σ (dash-dotted curve in Fig. 10) and the multiple equilibria are less likely to be relevant. In the latter case, a large interval of σ_r appears where the northern-sinking solution is the only steady state. In the realistic regime, the pattern as drawn in Fig. 11c is found that has the correct features of the present thermohaline ocean circulation. The solution where the NPP branch is unique, even for stronger asymmetry in the freshwater flux (Fig. 11c), remains similar to the NPP solution (Fig. 11a) in the range where a second equilibrium exists.

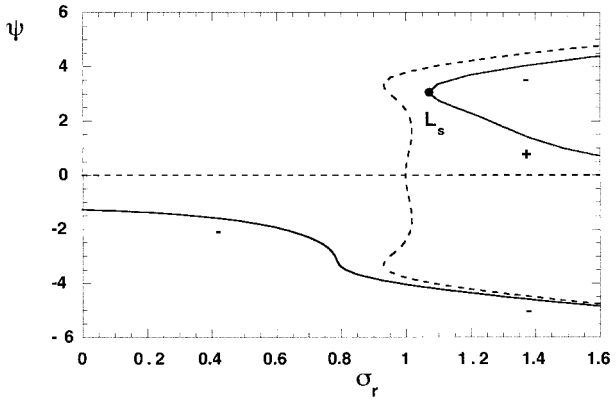

FIG. 6. Bifurcation diagram as in Fig. 4, but for the latitudinally asymmetric continental configuration of the standard case (γ given in Fig. 3b). The symmetric continental configuration case of Fig. 1 is given for comparison (dashed curves).

5. Summary and discussion

A simple coupled ocean–atmosphere model is used to study the effects of latitudinal asymmetry about the equator upon multiple equilibria of the thermohaline circulation. The primary source of asymmetry about the equator in the boundary conditions of the climate system is the configuration of the continents. We examine here two effects that produce asymmetry in the boundary conditions. The first arises because the high-latitude northern Atlantic Ocean occupies a smaller fraction of a latitude circle than the southern oceans; since warming of the Atlantic SST by ocean heat transport is less able to influence the atmospheric temperature, thermal driving of the THC tends to be more effective in the north. In observations, this effect is seen as cold continental

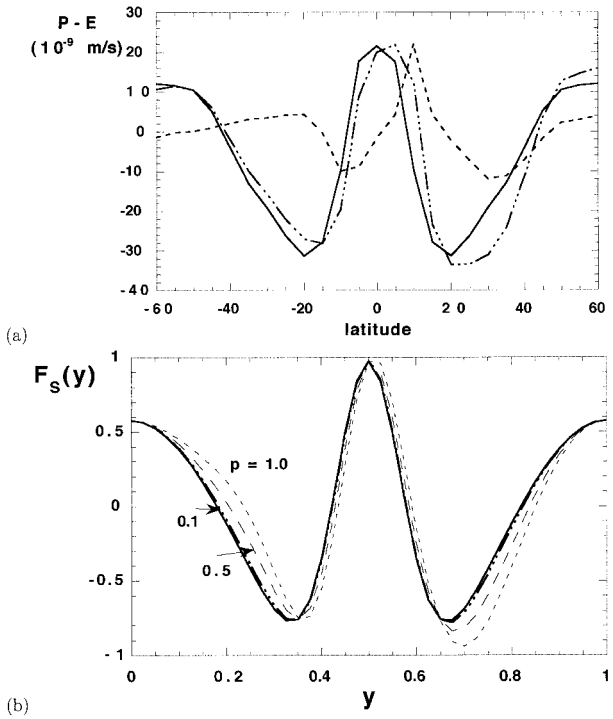

FIG. 7. Shapes of more realistic freshwater flux profiles used in this study. (a) The $P - E$ curve using the data of three zonally averaged profiles as discussed in the text (dash-dotted). The symmetric component of this flux is shown as the solid curve and the difference between the two is plotted as the dashed curve. (b) The solid curve shows the F_S^s latitude profile derived from the symmetric curve in Fig. 7a, corresponding to (12a). The other curves indicate F_S profiles as in (12b) as function of a parameter p that deforms the symmetric profile toward an approximation to the asymmetric observed profile (dash-dotted curve in Fig. 7a). Values of p are indicated.

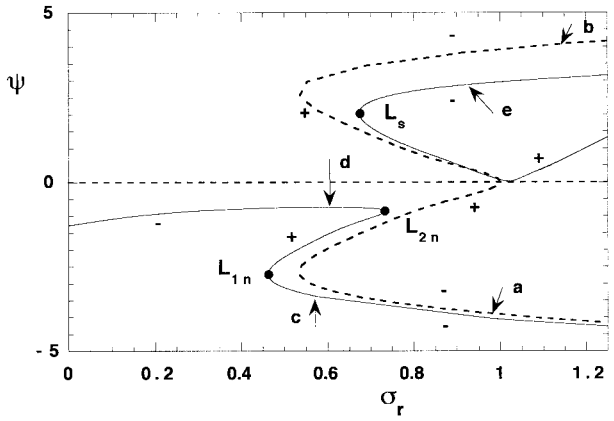

FIG. 8. Bifurcation diagrams (in the parameter σ_r governing the strength of freshwater flux) for freshwater flux latitudinal dependence similar to observed but symmetric about the equator, using the flux F_S in Fig. 7b with $p = 0$. Dotted curves show a case with symmetric continental configuration ($\gamma = 0.125$ independent of latitude). Solid curves show the case of standard continental configuration [$\gamma(y)$ as in Fig. 3b]. Limit points for this case are marked L_s, L_{1n}, L_{2n}; letters a–e show points for which solutions are plotted in Fig. 9.

winds blowing over the relatively limited ocean regions bordering the subpolar Atlantic, to produce strong convection. Here this is represented in a zonally averaged energy-balance atmosphere model affected by the ocean over a specified fraction of the domain. The second asymmetric effect in the boundary conditions is in the freshwater flux. In the observed climate system, this is related to the continental asymmetry that produces asymmetry in the atmospheric circulation, for example the position of the intertropical convergence zone, which is on average located slightly north of the equator. Here, we simply specify an approximation to observed freshwater flux and compare to a symmetrized version and to versions with reduced asymmetry.

Different meridional profiles of the fractional area of ocean, γ, were specified in the ocean–atmosphere model to determine the impact of this on the asymmetry in the equilibrium states. Our reference point has been the fully symmetric forcing case, where it is known that both southern-sinking (SPP) and northern sinking (NPP) pole to pole solutions exist through symmetry breaking of the symmetric thermally driven solution. When an asymmetry is imposed on the system, the pitchfork bifurcation responsible for symmetry breaking must disappear, breaking up into separate branches. Asymmetry in the continental configuration causes this breakup to occur rapidly, in the sense that the branches become well separated from the point of the pitchfork bifurcation even for modest asymmetry in the boundary conditions. Because the asymmetry has broken up the pitchfork in a way that favors northern sinking, the northern-sinking pole to pole branch and the thermally driven (TH) branch become one branch of solutions, which we term NPP/TH, while the southern-sinking branch (SPP) is separated. The connection of NPP and TH is typically associated with a pair of limit points that create a region of overlap between an asymmetric version of the TH branch and the NPP branch, so both equilibria exist over this range. The southern-sinking solution, on the other hand, can only be maintained at larger values of the magnitude σ of the freshwater flux forcing. Physically, this is because a larger area of air–sea interaction in the south means that the southward heat transports of the SPP solution are not as effectively opposed by the atmosphere as is the case for northward heat transports in the NPP solution. Greater salt advection effects are therefore required to overcome the effect of warming on the buoyancy of the upper ocean for the SPP solution. In terms of the bifurcation diagram, a limit point marks the minimum value of σ for which the SPP solution exists.

Introducing asymmetry in the freshwater flux reinforces the effects associated with the continental asymmetry. Even modest asymmetry approximating that observed produces a large impact on the southern-sinking branch, whose limit point shifts to high freshwater flux. No southern-sinking equilibrium is thus found in the realistic freshwater flux forcing regime. The asymmetric

freshwater flux freshens the southern part of the basin relative to the north, promoting northern sinking. The range of existence of the strong northern-sinking branch is thus extended, just as the range of σ for the southern-sinking branch is reduced. In much of the realistic range of parameters, the northern pole to pole circulation solution is the only equilibrium. We refer to this as the ''NPP-only regime'' of the parameter space.

Multiple equilibria occur within part of the realistic parameter range due to the two limit points on the NPP/TH branch. Such structures with pairs of limit points are sometimes refered to as hysteresis bifurcations. If the control parameter is varied slowly back and forth, the system goes through a hysteris loop with time. The two equilibria in this range are an NPP solution with strong overturning, and a TH solution that is asymmetric in latitude with a northern-sinking cell that is larger in extent and stronger than the southern cell, though weaker than the NPP overturning. We refer to this as the ''NPP + ATH regime.'' The range of coexistence of these two equilibria is reduced by increasing the asymmetry, but remains substantial for the realistic case.

Transitions between the NPP and ATH solutions are more plausible for rapid climate change than the transitions originally found in ocean models between NPP and SPP branches. Rahmstorf (1994) argued that paleoclimate data (notably Veum et al. 1992; Lehman and Keigwin 1992) are more consistent with a reduction in Atlantic overturning circulation than with a complete reversal to Southern Ocean sinking. Reconstructions of atmospheric radiocarbon concentration (Hughen et al. 1998) and east Atlantic deepwater circulation (Sarnthein et al. 1994) appear consistent with this, although Blumer et al. (1997) find evidence that the Northern and Southern Hemispheres were in antiphase during the Younger Dryas. The partial bifurcation structure inferred from hysteresis by Rahmstorf (1995) corresponds to the NPP/TH hysteresis bifurcation in our bifurcation diagram; that is, Rahmstorf's model is in the NPP + ATH regime listed above. The parameter used in Rahmstorf's study affects the meridional structure of the freshwater forcing (and has the inverse effect to ours, so obviously the diagram must be flipped), but can be viewed as a slightly different slice in parameter space through the surfaces of equilibrium solutions. Caution must, of course, be used in interpreting ocean GCM results in terms of two-dimensional ocean model solutions. Another source of multiple equilibria in three-dimensional models is associated with changes in the location of the convective zones within the subpolar Atlantic region (Lenderlink and Haarsma 1994; Rahmstorf 1994), and this cannot be properly captured in a zonally averaged model. However, we interpret these effects according to Rahmstorf's (1995) results as wrinkles in the NPP solution; the transition from these closely related variants of the NPP solution to a reduced overturning solution we interpret as a transition to the ATH branch.

The substantial range of the NPP-only regime raises the question of whether the asymmetries in the observed climate system might so favor the conveyor belt NPP solution that it is unique. Paleoclimate variations would then not be due to switching among very different THC equilibriums, except perhaps for among the modest variations on the NPP solution due to changes in the location of convection. Changes in the THC such as those noted in paleoclimate records can occur due to many other sources: changes in boundary conditions, stochastic forcing about a single equilibrium (e.g., Mikolajewicz and Maier-Reimer 1990; Mysak et al. 1993), and internal THC variability (Weaver et al. 1991, 1993; Stocker and Mysak 1992; Delworth et al. 1993, 1997; Marotzke 1994; Chen and Ghil 1995; and references therein). Indeed, Veum et al. (1992) argue based on timing considerations that switching between equilibriums of the THC could not have been the cause of either the termination of the last glacial maximum or the onset of the Younger Dryas. If the climate system is currently in the NPP-only regime, it would somewhat reduce the range of unknowns in THC-related effects to anticipate from anthropogenic climate change (Tziperman 1997). This question must be answered by more realistic models, but with the following considerations. (i) Flux correction—including the common practice of spinning up a model using restoring conditions to observed salinity, then diagnosing a salinity flux for use in mixed boundary condition integrations—tends to distort the range over which multiple equilibria occur (Dijkstra and Neelin 1999) and their stability properties (Nakamura et al 1994; Marotzke and Stone 1995; Marotzke 1996), and should not be used for evaluating existence of multiple equilibria, although it can be useful for other aims. (ii) Simple restoring boundary conditions on temperature tend to extend the range over which multiple equilibria are found (Tziperman et al 1994; Rahmstorf and Willebrand 1995), so some form of atmospheric model is required. (iii) The results here suggest that the small area of air–sea interaction in the North Atlantic is quite significant in providing asymmetry, so a model with realistic representation of this geometry is required. To our knowledge, the model that most closely meets these requirements in the literature reviewed here is Rahmstorf's (although the atmospheric component is simplified), so we must tentatively identify the NPP + ATH regime as ''most realistic.'' It is possible that some models have encountered the NPP-only regime but have chosen not to emphasize this in publications, since it appears less exciting. We would like to raise the challenge to modelers to evaluate more carefully the possibilty of the NPP-only regime.

Can we interpret the difference between Rahmstorf's results and those of Weaver and Hughes (1994), Marotzke and Willebrand (1991), and Stocker et al. (1992a), among others? A caveat is needed in that our two-dimensional model does not have a good simulation of coexisting Antarctic bottom water formation and intermediate water formation, which occurs in ocean GCMs;

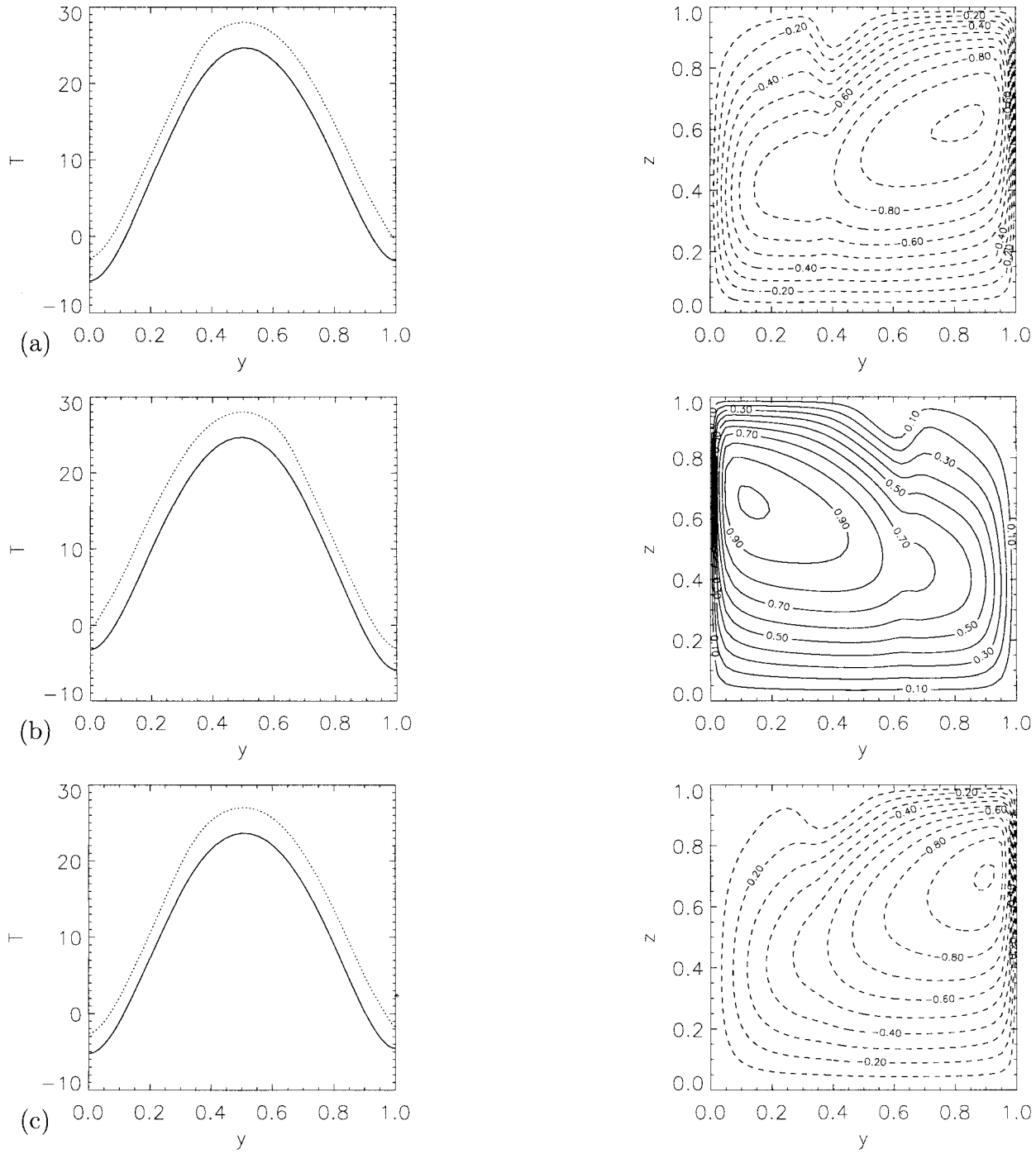

FIG. 9. Solutions at marked points in Fig. 8 for a case with realistic but symmetric freshwater flux and either symmetric or standard asymmetric continental configuration. Left panel shows sea surface temperature (dotted curve) and atmospheric surface temperature (solid curve). Right panel shows latitude–depth plots of the streamfunction, scaled by its absolute maximum; contour levels are with respect to this maximum. (a) NPP/TH branch, γ is constant, $\sigma_r = 1.16$. (b) SPP/TH branch, γ is constant, $\sigma_r = 0.92$. (c) NPP/TH branch, $\gamma(y)$ standard, $\sigma_r = 0.58$. (d) NPP/TH branch, $\gamma(y)$ standard, $\sigma_r = 0.60$. (e) SPP/TH branch, $\gamma(y)$ standard, $\sigma_r = 0.92$.

but the qualitative nature of the bifurcation diagram is likely to be fairly robust, and Stocker et al. (1992b) showed that such bottom water formation can be obtained by tuning boundary conditions without drastic changes to the overall solution. Other caveats include the simple model's lack of the dynamical effects of the Antarctic Circumpolar Current (e.g., Rahmstorf 1996; Toggweiler and Samuels 1998). The sources of asym-

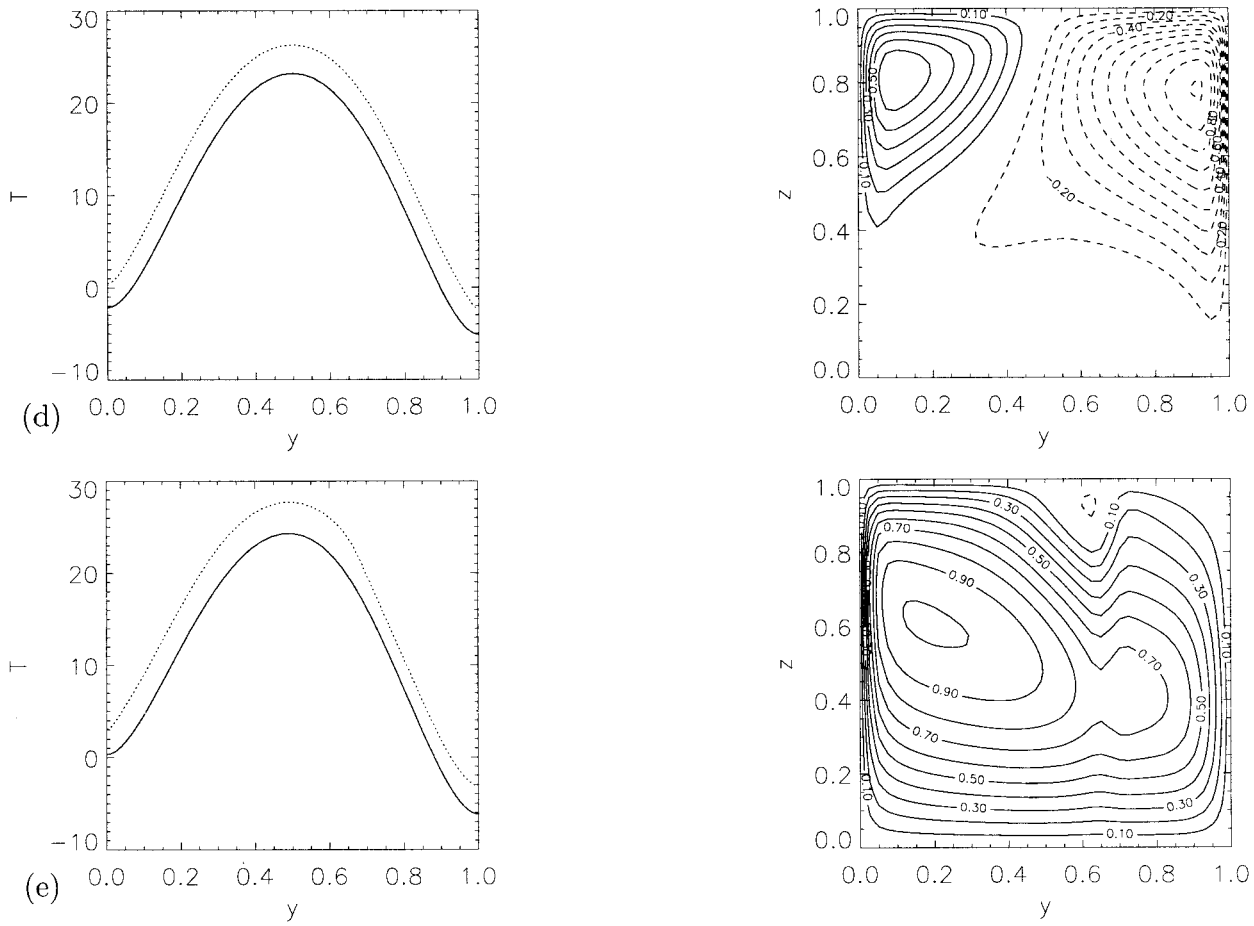

FIG. 9. (*Continued*)

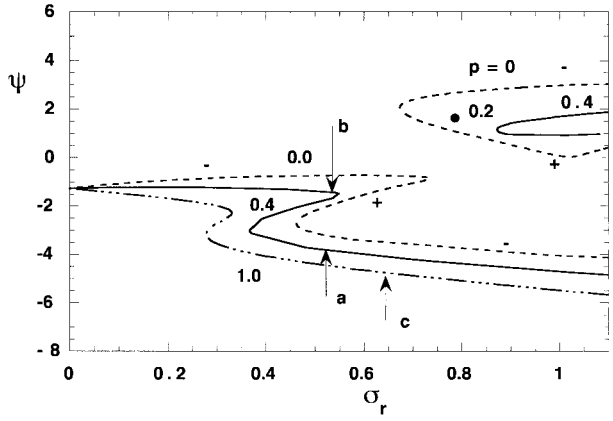

FIG. 10. Bifurcation diagram as in Fig. 8 for asymmetric standard case continental configuration [$\gamma(y)$ as in Fig. 3b] and for several values of p, measuring the degree of asymmetry of the freshwater flux (12b) according to Fig. 7b. The bifurcation diagram for $p = 0$ (symmetric freshwater flux) is the same as the solid curves in Fig. 8. The dot marks the position of the limit point L_s for $p = 0.2$. Letters a–c show points for which solutions are shown in Fig. 11.

metry will not be identical among models, but the qualitative behavior of the bifurcation diagram will tend to follow the example of the simple model. Weaver and Hughes (1994) obtained two equilibria corresponding to the SPP and NPP, respectively, with an additional weaker northern-sinking state (which may not have been a stable equilibrium). It appears that the Weaver–Hughes model falls into a regime that has NPP, ATH, and SPP states coexisting, similar to the central part of the bifurcation diagram in Fig. 8. This only occurs for weak asymmetry, and for more realistic asymmetry the only regimes with NPP-only or NPP + ATH equilibria exist. We conjecture that the asymmetry in their model is weaker than in Rahmstorf's because they use an idealized Atlantic basin of constant width, which reduces the asymmetry due to the ocean fraction affecting air–sea interaction. In the Weaver–Hughes model, flux correction has been used for the salinity field, apparently with the result that in the strongest overturning branch (NPP) is stronger than observed, while the ATH corresponds to the observed circulation. Marotzke and Willebrand (1991) used a model with interchangeable Pacific and Atlantic basins and thus obtained additional equilibria with Pacific sinking.

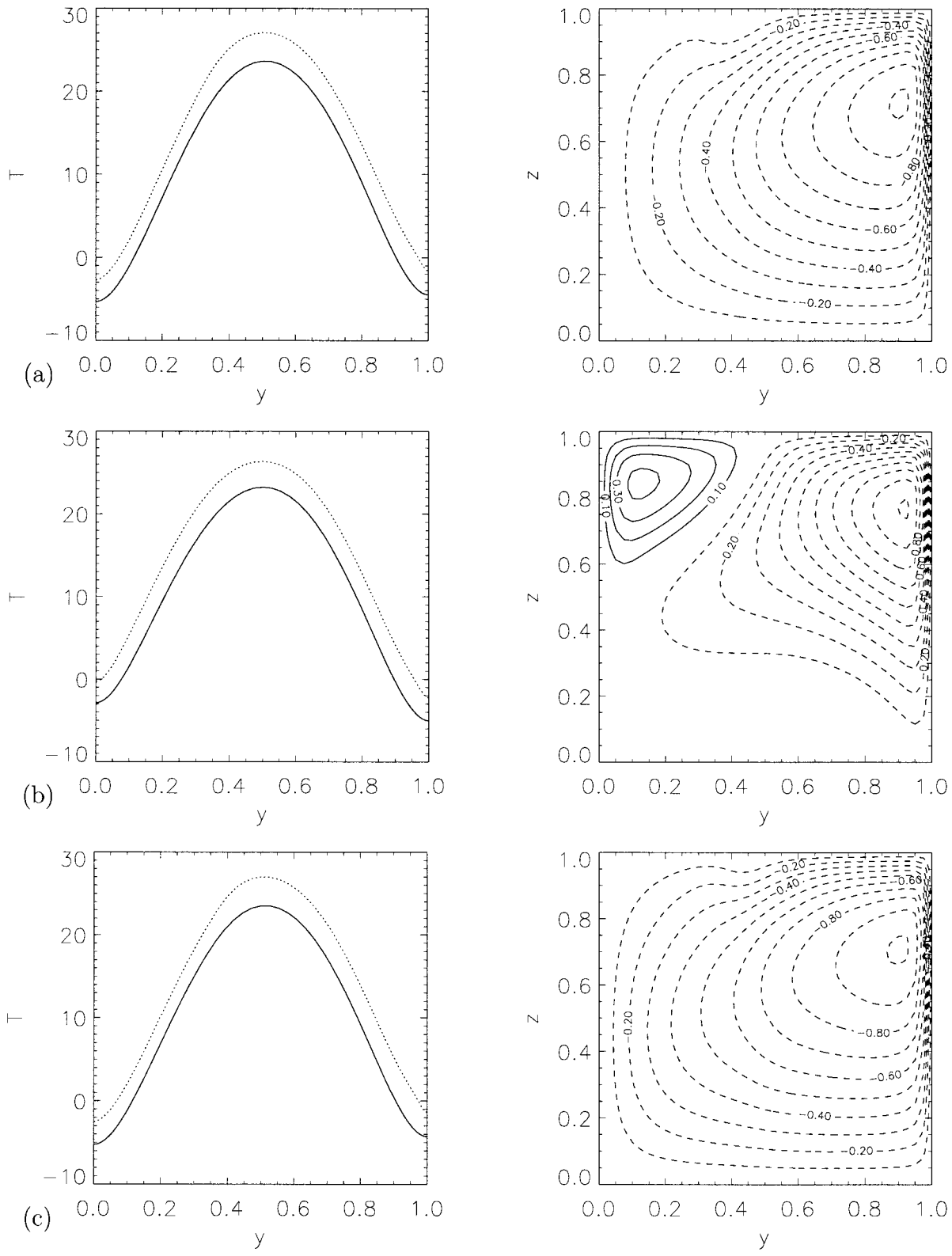

FIG. 11. Solutions at marked points in Fig. 10. Left panels show SST (dotted curve) and atmospheric surface temperature (solid curve). Right panels show latitude–depth plots of the streamfunction, scaled by its absolute maximum; contour levels are with respect to this maximum. (a) NPP/TH branch, $p = 0.4$, $\sigma_r = 0.51$. (b) NPP/TH branch, $p = 0.4$, $\sigma_r = 0.54$. (c) NPP/TH branch, $p = 1.0$, $\sigma_r = 0.64$.

So far as North Atlantic versus southern sinking is concerned, it appears their model corresponds most closely to the NPP + SPP regime, with no TH solution. A similar classification would apply to the Stocker et al. (1992a) model, although they include asymmetry effects due to the greater northward extent of the Atlantic. The narrow region of air–sea interaction in the North Atlantic is also neglected in these models and so omits this source of asymmetry.

The results above are only useful insofar as they can be verified by users of more complex models. We provide them as an example of how the asymmetric bifurcation diagrams may guide, or at least stimulate, experiments in GCMs. While details may differ in more complex models, we emphasize four main points from the results here.

1) Asymmetry about the equator due to continental configuration in the Atlantic and due to the freshwater flux both tend to produce a preference for northern-sinking solutions.
2) The separation of the SPP branch from the NPP/TH branch by these asymmetries can create a significant region of parameter space where there is no southern-sinking branch but where there is a conveyor belt NPP branch. The salt advection mechanism that was responsible for the bifurcation in the symmetric case acts to enhance the overturning of this NPP solution.
3) There is a region in the realistic part of parameter space with coexistence of the NPP branch and an asymmetric version of the thermally driven branch. However, when full asymmetry is included, there can also be a significant range of parameters where the NPP solution is unique and no multiple equilibria occur.
4) The role of the fractional region of air–sea interaction at each latitude on the heat flux feedback on the thermohaline circulation has been neglected in many studies but is substantial in this model. This effect of the continental configuration should be included, especially in the North Atlantic.

Acknowledgments. All computations were performed on the CRAY C90 at the Academic Computing Centre (SARA), Amsterdam, Netherlands, within project SC212 and SC498. Use of these computing facilities was sponsored by the National Computing Facilities Foundation with financial support from the Netherlands Organization for Scientific Research (NWO). This work was initiated and completed during visits of HD to UCLA in 1996 and 1997 and sponsored by NSF Grant ATM-9521389 and an NWO PIONIER-grant. Thanks are due to Richard Bintanja and Jan de Wolde (both IMAU) for providing the data for Fig. 3 and to Wilbert Weijer (IMAU) for providing the data in Fig. 7 and the freshwater flux fit Eq. (12a).

REFERENCES

Baumgartner, A., and E. Reichel, 1975: *The World Water Balance.* Verlag, 179 pp.

Blumer, T., and Coauthors, 1997: Timing of the Antarctic Cold Reversal and the atmospheric CO_2 increase with respect to the Younger Dryas event. *Geophys. Res. Lett.,* **24,** 2683–2686.

Broecker, W. S., 1993: The great ocean conveyor. *Oceanography,* **4,** 79–89.

——, D. M. Peteet, and D. Rind, 1985: Does the ocean–atmosphere system have more than one stable mode of operation? *Nature,* **315,** 21–26.

Bryan, F., 1986: High-latitude salinity effects and interhemispheric thermohaline circulations. *Nature,* **323,** 301–304.

Cessi, P., and W. R. Young, 1992: Multiple equilibria in two-dimensional thermohaline circulation. *J. Fluid Mech.,* **241,** 291–309.

Chen, F., and M. Ghil, 1995: Interdecadal variability of the thermohaline circulation and high-latitude surface fluxes. *J. Phys. Oceanogr.,* **25,** 2547–2560.

——, and ——, 1996: Interdecadal variability in a hybrid coupled ocean–atmosphere model. *J. Phys. Oceanogr.,* **26,** 1561–1578.

Delworth, T. L., S. Manabe, and R. J. Stouffer, 1993: Interdecadal variations of the thermohaline circulation in a coupled ocean–atmosphere model. *J. Climate,* **6,** 1993–2011.

——, ——, and ——, 1997: Multidecadal climate variability in the Greenland sea and surrounding regions: A coupled model simulation. *Geophys. Res. Lett.,* **24,** 257–260.

Dijkstra, H. A., and M. J. Molemaker, 1997: Symmetry breaking and overturning oscillations in thermohaline flows. *J. Fluid Mech.,* **331,** 169–198.

——, and J. D. Neelin, 1999: Imperfections of the thermohaline circulation: Multiple equilibria and flux-correction. *J. Climate,* **12,** 1382–1392.

Fanning, A. F., and A. J. Weaver, 1996: An atmospheric energy-moisture balance model: Climatology, interpentadal climate change, and coupling to an ocean general circulation model. *J. Geophys. Res.,* **101,** 15 111–15 128.

Haney, R. L., 1971: Surface thermal boundary condition for ocean circulation model. *J. Phys. Oceanogr.,* **1,** 241–248.

Huang, R. X., J. R. Luyten, and H. M. Stommel, 1992: Multiple equilibrium states in combined thermal and saline circulation. *J. Phys. Oceanogr.,* **22,** 231–246.

Hughen, K. A., J. T. Overpeck, S. J. Lehman, M. Kashgarian, J. Southon, L. C. Peterson, R. Alley, and D. M. Sigman, 1998: Deglaciation changes in ocean circulation from an extended radiocarbon calibration. *Nature,* **391,** 65–68.

Hughes, T. M. C., and A. J. Weaver, 1994: Multiple equilbria of an asymmetric two-basin ocean model. *J. Phys. Oceanogr.,* **24,** 619–637.

——, and ——, 1996: Sea surface temperature–evaporation feedback and the ocean's thermohaline circulation. *J. Phys. Oceanogr.,* **26,** 644–654.

Lehman, S. J., and L. D. Keigwin, 1992: Sudden changes in North Atlantic circulation during the last deglaciation. *Nature,* **356,** 757–762.

Lenderink, G., and R. J. Haarsma, 1994: Variability and multiple equilibria of the thermohaline circulation associated with deep-water formation. *J. Phys. Oceanogr.,* **24,** 1480–1493.

Manabe, S., and R. J. Stouffer, 1988: Two stable equilibria of a coupled ocean–atmosphere model. *J. Climate,* **1,** 841–866.

——, and ——, 1993: Century-scale effects of increased atmosphere CO_2 on the ocean–atmosphere system. *Nature,* **364,** 215–220.

——, and ——, 1995: Simulation of abrupt climate change induced by freshwater input to the North Atlantic Ocean. *Nature,* **378,** 165–167.

Marotzke, J., 1994: Ocean models in climate problem. *Ocean Processes in Climate Dynamics: Global and Mediterranean Examples,* P. Malanotte-Rizzoli and A. R. Robinson, Eds., NATO ASI Series C, Vol. 419, Kluwer, 79–109.

——, 1996: Analysis of thermohaline feedbacks. *Decadal Climate*

Variability: Dynamics and Predictability, D. L. T. Anderson and J. Willebrand, Eds., NATO ASI Series, Vol. I 44, Springer-Verlag, 333–378.

——, and J. Willebrand, 1991: Multiple equilibria of the global thermohaline circulation. *J. Phys. Oceanogr.*, **21,** 1372–1385.

——, and P. H. Stone, 1995: Atmospheric transports, the thermohaline circulation, and flux adjustments in a simple coupled model. *J. Phys. Oceanogr.*, **25,** 1350–1364.

——, and D. W. Pierce, 1997: On spatial scales and lifetimes of SST anomalies beneath a diffusive atmosphere. *J. Phys. Oceanogr.*, **27,** 133–139.

——, P. Welander, and J. Willebrand, 1988: Instability and multiple steady states in a meridional-plane model of thermohaline circulation. *Tellus*, **40A,** 162–172.

Mikolajewicz, U., and E. Maier-Reimer, 1990: Internal secular variability in an ocean general circulation model. *Climate Dyn.*, **4,** 145–156,

Mysak, L. A., T. F. Stocker, and F. Huang, 1993: Century-scale variability in a randomly forced, two-dimensional thermohaline circulation ocean circulation model. *Climate Dyn.*, **8,** 103–116.

Nakamura, M., P. H. Stone, and J. Marotzke, 1994: Destabilization of the thermohaline circulation by atmospheric eddy transports. *J. Climate*, **7,** 1870–1882.

North, G. R., R. F. Cahalan, and J. A. Coakley Jr., 1981: Energy balance climate models. *Rev. Geophys. Space Phys.*, **19,** 91–121.

Oort, A. H., 1983: *Global Atmospheric Circulation Statistics, 1885–1973*. NOAA Professional Paper 14, 180 pp.

Peixoto, J. P., and A. H. Oort, 1992: *Physics of Climate*. American Institute of Physics, 520 pp.

Power, S. B., and R. Kleeman, 1993: Multiple equilibria in a global ocean general circulation model. *J. Phys. Oceanogr.*, **23,** 1670–1681.

Quon, C., and M. Ghil, 1992: Multiple equilibria in thermosolutal convection due to salt-flux boundary conditions. *J. Fluid Mech.*, **245,** 449–484.

——, and ——, 1995: Multiple equilibria and stable oscillations in thermosolutal convection at small aspect ratio. *J. Fluid Mech.*, **291,** 33–35.

Rahmstorf, S., 1994: Rapid climate transitions in a coupled ocean–atmosphere model. *Nature*, **372,** 82–85.

——, 1995: Bifurcations of the Atlantic thermohaline circulation in response to changes in the hydrological cycle. *Nature*, **378,** 145–149.

——, 1996: On the freshwater forcing and transport of the Atlantic thermohaline circulation. *Climate Dyn.*, **12,** 799–811.

——, and J. Willebrand, 1995: The role of temperature feedback in stabilizing the thermohaline circulation. *J. Phys. Oceanogr.*, **25,** 787–805.

——, J. Marotzke, and J. Willebrand, 1995: Stability of the thermohaline circulation. *The Warm Water Sphere of the North Atlantic Ocean*, W. Krauss, Ed., Borntraeger, 129–158.

Sarnthein, M., K. Winn, S. J. A. Jung, J.-C. Duplessy, L. Labeyrie, H. Erlenkeuser, and G. Ganssen, 1994: Changes in east Atlantic deepwater circulation over the last 30 000 years: Eight time slice reconstructions. *Paleoceanography*, **9,** 209–267.

Stocker, T. F., and D. G. Wright, 1991a: Rapid transitions of the ocean's deep circulation induced by changes in surface water fluxes. *Nature*, **351,** 729–732.

——, and ——, 1991b: A zonally averaged ocean model for the thermohaline circulation. Part II: Interocean circulation in the Pacific–Atlantic basin system. *J. Phys. Oceanogr.*, **21,** 1725–1739.

——, and L. A. Mysak, 1992: Climate fluctuations on the century time scale: A review of high-resolution proxy data and possible mechanisms. *Climatic Change*, **20,** 227–250.

——, and A. Schmittner, 1997: Influence of CO_2 emission rates on the stability of the thermohaline circulation. *Nature*, **388,** 862–865.

——, D. G. Wright, and L. A. Mysak, 1992a: A zonally averaged, coupled ocean–atmosphere model for paleoclimate studies. *J. Climates*, **5,** 773–797.

——, ——, and W. S. Broecker, 1992b: The influence of high-latitude surface forcing on the global thermohaline circulation. *Paleoceanography*, **7,** 529–541.

Stommel, H., 1961: Thermohaline convection with two stable regimes of flow. *Tellus*, **13,** 244–230.

Thual, O., and J. C. McWilliams, 1992: The catastrophe structure of thermohaline convection in a two-dimensional fluid model and a comparison with low-order box models. *Geophys. Astrophys. Fluid Dyn.*, **64,** 67–95.

Toggweiler, J. R., and B. Samuels, 1998: On the ocean's large-scale circulation near the limit of no vertical mixing. *J. Phys. Oceanogr.*, **28,** 1832–52.

Tziperman, E., 1997: Inherently unstable climate behavior due to weak thermohaline ocean circulation. *Nature*, **386,** 592–595.

——, J. R. Toggweiler, Y. Feliks, and K. Bryan, 1994: Instability of the thermohaline circulation with respect to mixed boundary conditions: Is it really a problem for realistic models? *J. Phys. Oceanogr.*, **24,** 217–232.

Vellinga, M., 1996: Instability of two-dimensional thermohaline circulation. *J. Phys. Oceanogr.*, **26,** 305–319.

——, 1998: Multiple equilibria in ocean models as a side effect of convective adjustment. *J. Phys. Oceanogr.*, **28,** 621–633.

Veum, T., E. Jansen, M. Arnold, I. Beyer, and J.-C. Duplessy, 1992: Water mass exchange between the North Atlantic and the Norwegian Sea during the past 28 000 years. *Nature*, **356,** 783–785.

Weaver, A. J., and E. S. Sarachik, 1991: The role of mixed boundary conditions in numerical models of the ocean's climate. *J. Phys. Oceanogr.*, **21,** 1470–1493.

——, and T. M. Hughes, 1992: Stability and variability of the thermohaline circulation and its link to climate. *Trends in Physical Oceanography*, Research Trends Series, Council of Scientific Research Integration, 56 pp.

——, and ——, 1994: Rapid interglacial climate fluctuations driven by North Atlantic Ocean circulation. *Nature*, **367,** 447–450.

——, E. S. Sarachik, and J. Marotzke, 1991: Freshwater flux forcing of decadal and interdecadal oceanic variability. *Nature*, **353,** 836–838.

——, J. Marotzke, P. F. Cummings, and E. S. Sarachik, 1993: Stability and variability of the thermohaline circulation. *J. Phys. Oceanogr.*, **23,** 39–60.

Weijer, W., W. P. M. de Ruijter, H. A. Dijkstra, and P. J. van Leeuwen, 1999: Impact of interbasin exchange on the Atlantic overturning circulation. *J. Phys. Oceanogr.*, **29,** 2266–2284.

Welander, P., 1986: Thermohaline effects in the ocean circulation and related simple models. *Large Scale Transport Processes in Oceans and Atmosphere*, J. Willebrand and D. L. T. Anderson, Eds., D. Reidel, 163–200.

Winton, M., 1997: The effect of cold climate upon North Atlantic Deep Water formation in a simple ocean–atmosphere model. *J. Climate*, **10,** 37–51.

Zaucker, F., T. F. Stocker, and W. S. Broecker, 1994: Atmospheric freshwater fluxes and their effect on the global thermohaline circulation. *J. Geophys. Res.*, **99** (C6), 12 443–12 457.

Zhang, S., R. J. Greatbatch, and C. A. Lin, 1993: A re-examination of the polar halocline catastrophe and implications for coupled ocean–atmosphere modeling. *J. Phys. Oceanogr.*, **23,** 287–299.